Matter

CellPress

Article

Dynamically preferred state with strong electronic fluctuations from electrochemical synthesis of sodium manganate

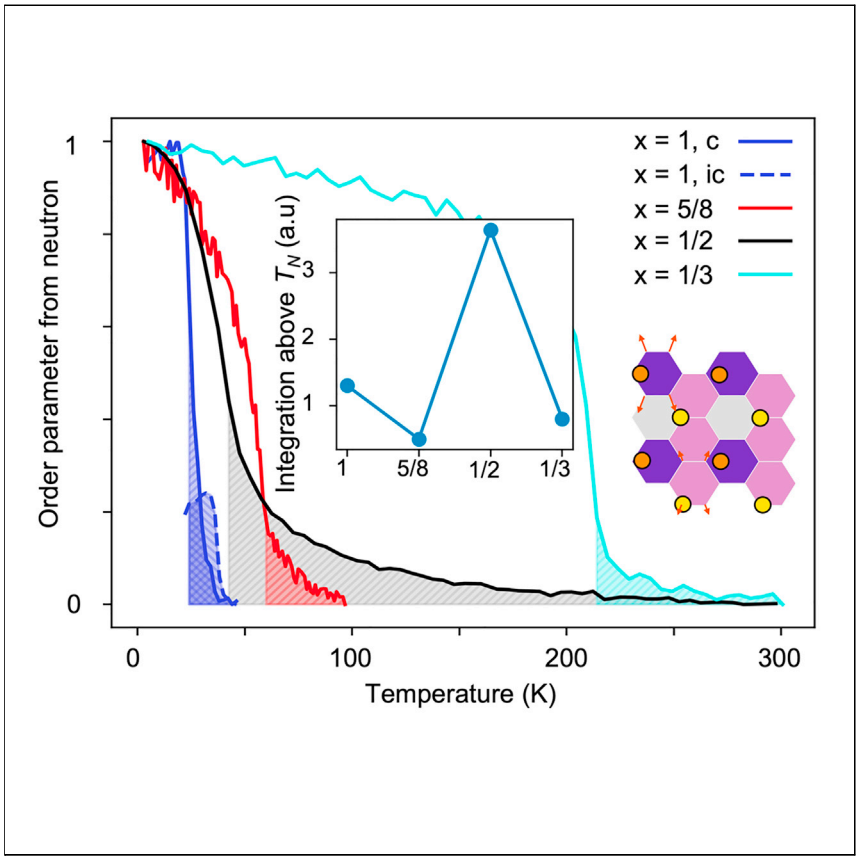

Electrochemical (de)intercalation is a delicate method to precisely control the composition and possible orderings of alkaline ions in alkaline transition metal oxides. Electrochemically prepared $Na_{1/2}MnO_2$ ordering exhibits abnormal structure distortions, charge orderings, and dynamic activities. Strong magnetic fluctuations and lattice dynamics are observed in an unusually wide temperature range, mediated through the unique charge flux oscillation. Our findings provide a new paradigm to understand how lattice dynamics can contribute to spin fluctuations through charge flux functionals on top of charge density functionals.

3 Understanding
Dependency and conditional studies on material behavior

Xi Chen, Yichao Wang, Yiping Wang, ..., Kenneth Burch, Jeffrey W. Lynn, Xin Li

lixin@seas.harvard.edu

Highlights

$Na_{1/2}MnO_2$ shows strong magnetic fluctuations and anharmonic phonons in experiments

DFT, XRD, Raman, and neutron reveal a unique dynamic metastable phase

Magnetic and phonon dynamics are linked by charge fluxes in $Na_{1/2}MnO_2$

Chen et al., Matter 5, 1–16
February 2, 2022
https://doi.org/10.1016/j.matt.2021.12.012

Please cite this article in press as: Chen et al., Dynamically preferred state with strong electronic fluctuations from electrochemical synthesis of sodium manganate, Matter (2021), https://doi.org/10.1016/j.matt.2021.12.012

Matter

CellPress

Article

Dynamically preferred state with strong electronic fluctuations from electrochemical synthesis of sodium manganate

Xi Chen,[1] Yichao Wang,[1] Yiping Wang,[2] Rebecca L. Dally,[3] Kamila Wiaderek,[4] Tianyu Qiao,[1] Jue Liu,[5] Enyuan Hu,[6] Kenneth Burch,[2] Jeffrey W. Lynn,[3] and Xin Li[1,7,*]

SUMMARY

Electrochemical (de)intercalation is a delicate method to precisely control the alkaline ion composition in alkaline transition metal oxides. Because of complicated interactions, metal charge ordering patterns can form spontaneously at special fractional alkaline compositions and orderings. Here, we show that this elegant electrochemical process can create dynamically preferred structures in an anharmonic energy landscape that conventional syntheses and computations can rarely visit. Specifically, electrochemically prepared $Na_{1/2}MnO_2$ ordering exhibits abnormal structure distortions, charge orderings, and dynamical activities. Strong magnetic fluctuations and lattice dynamics are observed in an unusually wide temperature range in $Na_{1/2}MnO_2$, which distinguishes it from all other Na_xMnO_2 at higher or lower Na compositions. The results emphasize the unique opportunity of using electrochemical processes to design and create novel quantum states with strongly coupled and mutually enhanced electronic and lattice fluctuations, likely through a special dynamic charge flux functional, as suggested by our computational investigations.

INTRODUCTION

$NaTMO_2$ (TM = 3*d* transition metals) compounds have been studied widely as battery electrode materials.[1–3] Importantly, they also often provide unique prototypical materials where important quantum effects emerge from strong electronic correlations.[4–8] Here we first identify the uniqueness of a $Na_{1/2}MnO_2$ ordered phase with abnormal Jahn-Teller (JT) distortions through a systematic structure analysis and comparison of all electrochemically prepared Na_xTMO_2 (TM = late 3*d* transition metals of Mn, Ni, Co, $0 < x \leq 1$), by (*in situ*) synchrotron X-ray diffraction (SXRD) and neutron diffraction measurements, combined with density functional theory (DFT) simulations. We then unveil an anomaly in temperature dependence of anharmonically coupled phonons in $Na_{1/2}MnO_2$ from base temperature to 300 K in Raman spectroscopy measurements and DFT simulations. A long-range magnetic ordering below the Néel temperature (T_N) at 47 K is also observed in neutron diffraction measurements, with the magnetic ordering consistent with DFT predictions and the T_N corresponding well to the temperature of Raman anomalies. A strong magnetic fluctuation above T_N emerges from the neutron order parameter analysis of $Na_{1/2}MnO_2$, which extends in an abnormally wider temperature range, compared with samples of Na_xMnO_2 at x = 1, 5/8, 1/3 obtained by the same synthesis method. Inelastic neutron scattering measurements show that the spin gap of $Na_{1/2}MnO_2$ closes above T_N, with strong magnetic fluctuations above the long-range ordered state because of short-range magnetic correlations.[8–12]

Progress and potential

Sodium (Na)-ordering phases can form spontaneously at special sodium compositions in layered sodium transition metal oxides in Na-ion batteries. Strong electronic correlation phenomena can emerge from these phases, including unconventional superconductivity, metal-insulator transition near room temperature, and an enhanced thermoelectric effect. Our study of $Na_{1/2}MnO_2$, an Na-ordering, dynamically metastable phase, reveals an unusually strong magnetic fluctuation that is robust against temperature increase up to room temperature. The underlying novel mechanism of strongly coupled lattice and spin oscillations mediated through the unique charge flux oscillation prompts a new way to think about how lattice dynamics can contribute to spin fluctuations. This may also provide a new perspective to understand other strongly correlated materials, including unconventional superconductors and other energy conversion and storage materials.

Please cite this article in press as: Chen et al., Dynamically preferred state with strong electronic fluctuations from electrochemical synthesis of sodium manganate, Matter (2021), https://doi.org/10.1016/j.matt.2021.12.012

Our analysis suggests that there is an important interplay between structure instability and anharmonic stabilization in $Na_{1/2}MnO_2$ that provides and connects the observed vibrant electronic and lattice dynamics. Specifically, our DFT simulation unveils that there are strong dynamic charge transfers between ions, or charge fluxes, that are more confined in the $Mn^{3.5+}O_6$ charge stripe region (or simply the stripe region) of $Na_{1/2}MnO_2$ than in other regions of the crystal. Here a higher level of "confinement" means that the charge flux happens more within the geometric space defined by the stripe region. More importantly, we find that these charge fluxes in $Na_{1/2}MnO_2$ much more effectively modulate the dynamical coupling of charge, lattice, and magnetic interactions than Na_xMnO_2 at other Na compositions. DFT simulations show that dominant magnetic exchange constants can be transiently modulated by strongly coupled anharmonic phonons through such charge fluxes, which suggests that anharmonic phonon coupling and magnetic exchange could be functionals of the entire transient distribution of charge fluxes, in analogy to the more familiar construction of energies being considered as functionals of charge density distribution in DFT. The dynamic emergent phenomenon and related methodology found in the model system of $Na_{1/2}MnO_2$ here thus provides a new perspective and paradigm, focused on the charge flux[13] functional on top of the conventional charge density functional, to further understand other strongly correlated materials, with amplified or new functionality often approaching structure instabilities, such as perovskite solar cell materials[14] and nickelate and cuprate superconductors.[15,16]

RESULTS AND DISCUSSION

Late-3*d* transition metals can, in principle, show JT activity[17,18] in the TMO_6 octahedron of layered Na_xTMO_2, when the e_g orbitals are partially occupied, such as for Mn^{3+} and Ni^{3+}. Depending on whether dx^2-y^2 or dz^2 orbitals are occupied, the octahedron can show compressed (4 long and 2 short Mn-O bonds) or elongated (2 long and 4 short) tetragonal local symmetry, also called negative or positive JT distortion modes, respectively. At x = 1, the synthesized Na_xTMO_2 compounds all show the O3 oxygen layer stacking (ABCABC stacking),[19] which contains the fundamental configuration with the two elongated JT long axes in the positive $Mn^{3+}O_6$ or $Ni^{3+}O_6$ octahedron pointing directly toward Na ions. Strong Na-Mn-O orbital interactions have been found in such a configuration, which manifest through the robustness of such or similar configurations identified in the ordering patterns of Na_xMnO_2 throughout the Na deintercalation in a wide Na composition range of $1/18 \leq x \leq 1$, with the stacking always kept at O3 at $1/3 \leq x \leq 1$.[7,20] However, upon Na deintercalation in the other late-3*d* Na_xTMO_2, which can reach a Na composition down to x = 1/3 (e.g., TM = Ni, Co), this Na-TM-O configuration has to be modified significantly because the oxygen stacking is changed spontaneously to P3 (AABBCC)[19] at around $1/2 \leq x \leq 2/3$.[21] The special O3-Na_xMnO_2 phase thus becomes the only late-3*d* $Na_{1/2}TMO_2$ that can show a stable O3 stacking near half Na composition in Na deintercalation. Previous works have studied the phase evolutions in these Na_xTMO_2 through computations[21,22] or experiments.[7,20,23,24]

Here we first present a systematic comparison of the phase evolution in Na_xTMO_2 (TM = Mn, Ni, Co, $0 < x \leq 1$), determined by *in situ* SXRD refinements (Figure 1A), where a Na-ion battery was cycled for electrochemical (de)intercalation with continuous Na composition change in an *in situ* battery cell with X-ray transparent windows on both electrode sides while SXRD patterns were taken simultaneously in transmission mode to monitor the structure evolution. The refinements (Figures S1–S6) of the

[1]School of Engineering and Applied Sciences, Harvard University, Cambridge, MA 02138, USA

[2]Department of Physics, Boston College, Boston, MA 02467, USA

[3]NIST Center for Neutron Research, National Institute of Standards and Technology, Gaithersburg, MD 20899, USA

[4]Advanced Photon Source, Argonne National Laboratory, Argonne, IL 60439, USA

[5]Neutron Scattering Division, Oak Ridge National Laboratory, Oak Ridge, TN 37831, USA

[6]Chemistry Division, Brookhaven National Laboratory, Upton, NY 11973, USA

[7]Lead contact

*Correspondence: lixin@seas.harvard.edu

https://doi.org/10.1016/j.matt.2021.12.012

Please cite this article in press as: Chen et al., Dynamically preferred state with strong electronic fluctuations from electrochemical synthesis of sodium manganate, Matter (2021), https://doi.org/10.1016/j.matt.2021.12.012

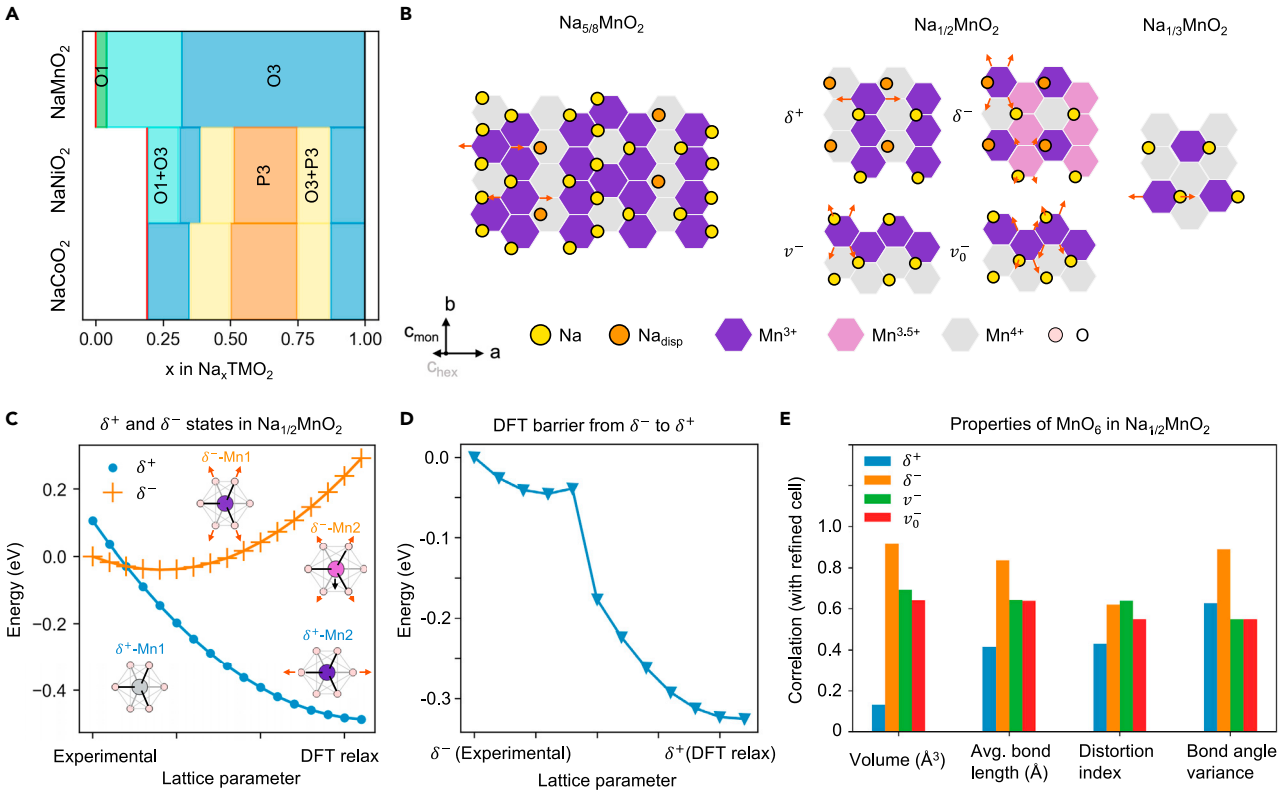

Figure 1. Phase evolution of Na_xTMO_2 (TM = Mn, Ni, Co) with Na composition (x) and abnormal JT distortions of O3-$Na_{1/2}MnO_2$

(A) Phase diagrams of $NaMnO_2$, $NaNiO_2$, and $NaCoO_2$ obtained from *in situ* SXRD measurements (Figures S1–S8). Black and red vertical lines on the boundaries mark the Na composition range in the *in situ* measurements.

(B) Evolution of the Na and Mn charge orderings for x = 5/8, 1/2, and 1/3 in Na_xMnO_2. Four candidate structures, δ^+, δ^-, v^-, and v_0^-, are found in DFT simulations for x = 1/2. JT distortions are indicated by red arrows, with the distortion level illustrated using arrow length.

(C) DFT energies of the δ^+ and δ^- states in $Na_{1/2}MnO_2$. The lattice parameters are interpolated between experimental lattice parameters determined by *in situ* SXRD refinement and DFT fully relaxed lattice parameters of the δ^+ state. The main distortions of MnO_6 octahedra for the two states are illustrated by red arrows in the insets. The black arrow indicates the $Mn^{3.5+}$ ion away from the perfect octahedron center to form the dimer in δ^-.

(D) DFT calculation of structures with gradually changing lattice parameters from the experimental value to the DFT fully relaxed value of δ^+. Each image has fixed lattice parameters, and the internal coordinates are relaxed.

(E) The correlation of the volumes, average bond lengths, distortion indices (which measure the difference in Mn-O bond lengths), and bond angle variances of all MnO_6 octahedra in $Na_{1/2}MnO_2$, between each of the four DFT candidate states and the state from *in situ* SXRD refinement of internal coordinates and lattice parameters, all at experimental lattice parameters.

in situ SXRD patterns (Figures S7 and S8) identify three major Na ordering phases for Na_xNiO_2 and Na_xCoO_2 at x = 2/3, 1/2, and 1/3, whereas our previous reports identified orderings at x = 5/8, 1/2, and 1/3 for Na_xMnO_2.[7,20] The specific Na ordering patterns solved from our *in situ* SXRD are shown in Figure S9, together with their stackings. The phase diagram in Figure 1A summarizes the information of stacking evolution of Na_xNiO_2, Na_xCoO_2, and Na_xMnO_2, which is largely consistent with previous results for TM = Mn[7,20,22] and Co,[21] and previous experiment[23] and our own DFT simulations for TM = Ni (Figure S10). Starting from the same O3 stacking at x = 1, the three materials, however, start to show very different orderings and stackings around x = 2/3–5/8, with TM = Mn keeping the O3 stacking and TM = Ni and Co showing a transformation to P3 stacking instead. But at x = 1/3, all three materials merge into the same Na ordering and O3 stacking (Figure S9). We want to emphasize again that the comparison unveils a unique property of Na_xMnO_2 to stay in the O3 phase and avoid the P3 phase in the entire phase evolution down to x = 1/3,

Please cite this article in press as: Chen et al., Dynamically preferred state with strong electronic fluctuations from electrochemical synthesis of sodium manganate, Matter (2021), https://doi.org/10.1016/j.matt.2021.12.012

including both Na orderings at x = 1/2 and x = 1/3, whereas Ni and Co systems show the P3 phase at $1/2 \leq x \leq 2/3$.

The focus of this work is on the unusual state of O3-$Na_{1/2}MnO_2$, which exhibits abnormal JT distortions and charge ordering. Figure 1B shows the structure evolution of main phases in Na_xMnO_2 upon electrochemical deintercalation of Na at x = 5/8, 1/2, and 1/3. At x = 1/2, DFT simulations found multiple competitive states of δ^+, δ^-, v^-, and v_0^-. The v_0^- phase is the DFT ground state, where the subscript "0" is for the ground state; the superscript "–" is for negative JT distortion of the $Mn^{3+}O_6$ octahedron, as illustrated by red arrows; and "v" is for "normal" octahedral Na sites that all Na ions occupy in the structure, as illustrated by yellow balls. However, previous work[20] found that, in $Na_{1/2}MnO_2$, there exists significant amount of Na ions at the displaced Na site (Na_{disp}) that are shifted halfway between two normal sites along the *b* direction (Figure S11A) with a different local environment than the normal Na site based on XRD refinements, very similar to the Na_{disp} sites first found in $Na_{5/8}MnO_2$.[7] This detail suggests that the experimental structure of $Na_{1/2}MnO_2$ should at least include the δ^+ or the δ^- states, where "δ" is for "displaced" Na_{disp} sites, as illustrated by orange balls, whereas the superscript "+" and "–" are for positive and negative JT distortions of $Mn^{3+}O_6$, respectively.

We thus performed refinement of *in situ* SXRD at x = 1/2 on the lattice parameters, with internal coordinates fixed at those from the DFT δ^+, δ^-, v^-, and v_0^- states, and obtained goodness-of-fit R_{wp} (weighted profile *R*-factor) of 5.089, 4.849, 4.941, and 4.920, respectively (see Experimental procedures and Figures S11B–S11D for more information). These numbers are relatively close to the R_{wp} of 3.51[19] from the full refinement, including the lattice parameters and internal coordinates. Furthermore, the refinement difference among these states is actually small, although δ^- is slightly better than others. Because structural evolution from one state to another among the four structures just needs some local Na shift along the *b* direction together with the local charge transfer between Mn ions, as can be seen easily in Figure 1B, the SXRD refinement results here cannot inarguably distinguish δ^+ from δ^- or exclude the possibility of their coexistence with v^- or v_0^-. We will thus present neutron diffraction, including the measured magnetic ordering, and neutron pair distribution function (nPDF) results later to demonstrate the preference for δ^- over δ^+ as well as the electronic and magnetic fluctuation results from the band and lattice dynamics in DFT simulations and the temperature evolution of neutron diffractions to emphasize the importance of the δ^- state over the other three states.

However, we first provide some evidence favoring the δ^- state, based mainly on a more detailed comparison of DFT simulations with *in situ* SXRD refinements, to make the readers more familiar with these structures. Figure 1C shows that, approaching experimental lattice parameters, δ^- becomes energetically competitive, not only in absolute energy values but, more importantly, showing a local energy minimum that δ^+ lacks. The DFT δ^- state exhibits the anomaly of a weakly compressed $Mn^{3.5+}O_6$ octahedron (δ^--Mn2 in Figure 1C) with actually comparable lengths in the six Mn-O bonds and obvious $Mn^{3.5+}$ dimerization along the pure $Mn^{3.5+}$ charge stripe in the *b* direction (pink stripe in Figure 1B). The neighboring $Mn^{3+/4+}$ *b* stripes (stripe with mixed purple and grey hexagons in Figure 1B) show strongly compressed $Mn^{3+}O_6$ (δ^--Mn1 in Figure 1C) with negative JT distortions. δ^+, on the contrary, exhibits only $Mn^{3+}O_6$ with strong positive JT distortions. Note that the lattice parameters *a*, *b*, and *c*, including β, of the δ^-state after DFT relaxation are very close to the experimental ones from SXRD refinement, whereas those of the δ^+ state are not (Figure S11C). We thus evolve total energies in DFT simulations from

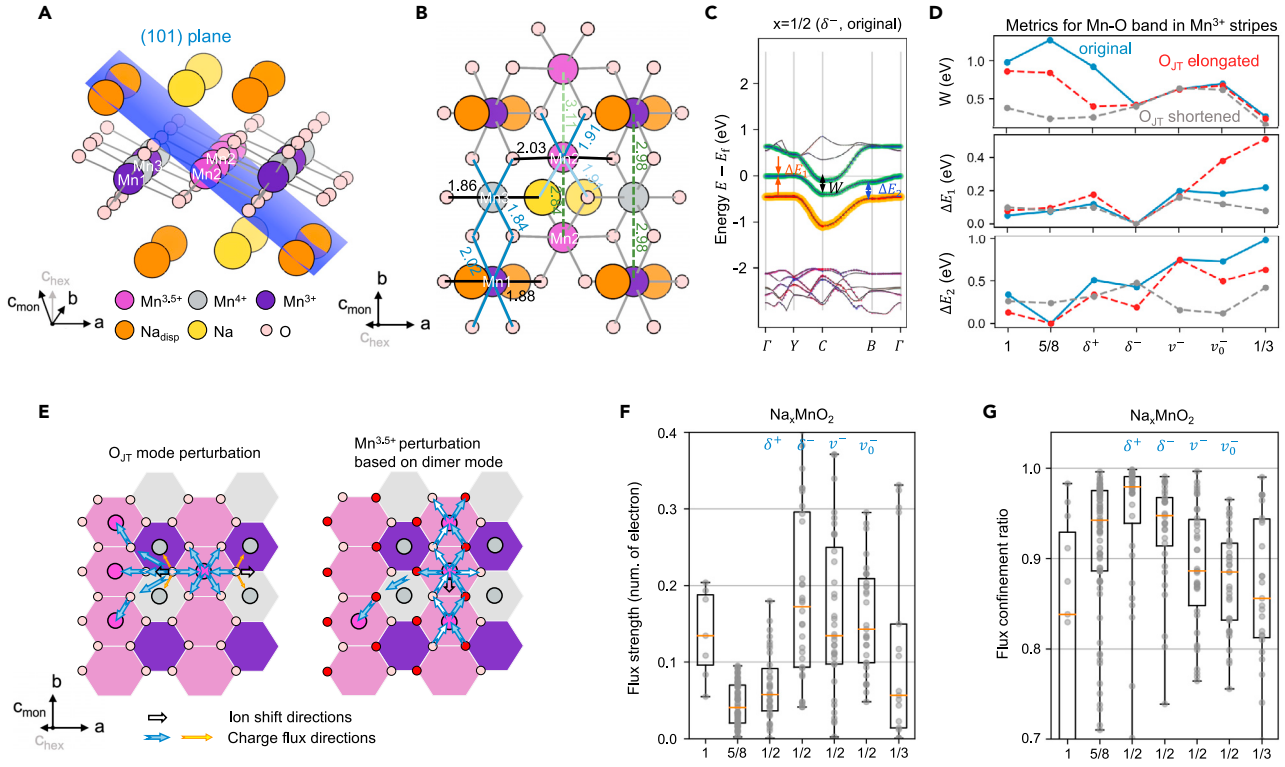

Figure 2. Dynamic electronic structures and charge fluxes of δ^--$Na_{1/2}MnO_2$ compared with other Na_xMnO_2

(A and B) 3D structure model of $Na_{1/2}MnO_2$ viewing around the *b* direction (A) and along the hexagonal *c* direction (B). The numbers show the bond length in angstroms.

(C) Band structure of the δ^- state of $Na_{1/2}MnO_2$. Green and blue markers represent the band occupation of the Mn *d* and the O *p* orbitals, respectively, in the JT active $Mn^{3.5+}O_6$ charge stripe. The color near E_f blends blue and green, indicating *pd* hybridization. The orange and red markers represent the band occupation of the Mn^{3+} $d_{x^2-y^2}$ and p_x or p_y orbitals of the four oxygens in the $d_{x^2-y^2}$ directions, respectively, in the $Mn^{3+}O_6$ of the $Mn^{3/4+}$ stripe. The band structures for all other states (x = 1, 1/3, and 5/8; δ^+, v_0^-, and v^-) and after ionic perturbation are shown in Figure S13.

(D) Metrics regarding the Mn-O hybridized bands for each of the seven Na_xMnO_2 states, including the band width (*W*), the smallest energy differences among all *k* directions to the Fermi level (ΔE_1) and to the lower bands (ΔE_2), for the original ones (blue) and perturbed ones, with two O_{JT} ions elongated (red) and shortened (grey). If the hybridized bands overlap with the Fermi level or any other bands, the energy difference is defined as zero.

(E) Charge fluxes in the MnO_2 plane after elongating a pair of O_{JT} (black empty arrow) around $Mn^{3.5+}$ (left) and perturbing a $Mn^{3.5+}$ ion along the *b* direction (right) from DFT simulations. Blue arrows mark fluxes inside the $Mn^{3.5+}O_6$ stripe region, and orange arrows mark fluxes leaked outside.

(F) Absolute flux strength value in the stripe region generated by different phonon modes (gray dots) in Na_xMnO_2 with a frequency larger than 300 cm^{-1} (37 meV).

(G) Flux confinement ratio of the stripe region under phonon mode perturbations in Na_xMnO_2. The middle 50% values are covered by the rectangles, with the orange bars marking the mean value.

the δ^- state at experimental lattice parameters that are nearly equivalent to DFT relaxed ones to δ^+ with a very different DFT relaxed lattice parameters (Figure 1D), which shows a small local barrier to overcome.

The δ^- state also shows the highest structure correlation, in Figure 1E, with the structure from our SXRD refinement of electrochemically prepared $Na_{1/2}MnO_2$[20] because of the structure details of Mn dimerization, the bond length and angle in the special distortions of MnO_6 octahedra, and the spatial distribution of these octahedra. The refined structure of $Na_{1/2}MnO_2$ is shown in Figures 2A and 2B, whereas the four DFT structures of v_0^-, v^-, δ^+, and δ^- at x = 1/2 are shown in Figure S11. However, it is worth noting that, contrary to $Na_{5/8}MnO_2$,[7] and the δ^+ state at x = 1/2,[20] where Na_{disp} is at the local minimum, Na_{disp} in δ^- indeed stays at the saddle point, suggesting that the existence of δ^- in the experiment may rely on certain dynamical effects.[14] In

Please cite this article in press as: Chen et al., Dynamically preferred state with strong electronic fluctuations from electrochemical synthesis of sodium manganate, Matter (2021), https://doi.org/10.1016/j.matt.2021.12.012

addition, for Na_xMnO_2 at x = 5/8 and 1/3 orderings, we confirmed that no such complexity from competing states in DFT exists. The ground-state structures from DFT simulations at x = 5/8 and 1/3 are fully consistent with SXRD refinements,[7,20] and all show strongly elongated positive JT distortions (Figures 1B and S12).

The DFT δ^- state at x = 1/2 shows unique static electronic structures (Figure 2C), as well as the dynamic ones under ionic perturbations, compared with other states at x = 1, 5/8, 1/2, and 1/3 (Figures 2D and S13). The δ^- state is the only structure with the top band passing through the Fermi level (E_f) and, hence, with a partial occupancy for a more collective behavior of charge carriers ($\Delta E_1 = 0$). The band is from *pd* hybridization of the unique weakly compressed $Mn^{3.5+}O_6$, which is well separated from bottom bands (ΔE_2 = 0.2–0.4 eV), suggesting little intermixing with other bands. The band also shows a reasonably wide band width (W = 0.42 eV), indicating that electrons will not be strongly localized. At x = 1/3, W is much narrower with much larger ΔE_1 and ΔE_2, suggesting strong electron localization; at x = 1 and 5/8, W is much wider with ΔE_2 almost closed, suggesting strong delocalization and band intermixing (see blue original lines in Figure 2D and more details in Figure S13). The results are consistent with the density of states (DOS) analysis (Figure S14).

Furthermore, we find that, for the structures at x = 1, 5/8, and 1/2 (δ^+) with clear Mn^{3+} stripes (purple straight stripes along the *b* direction in Figure 1B), ionic perturbations in DFT tend to generate a large change of W, whereas for structures at x = 1/3, ΔE_1 and ΔE_2 are more sensitive to such perturbations. The electronic structure of the δ^- state at x = 1/2 is, however, relatively robust against ionic perturbations. These trends are clearly illustrated in Figure 1D by the red and grey curves for W, ΔE_1, and ΔE_2 being perturbed by elongating or shortening a pair of oxygens in the Mn-O bonds corresponding to the elongated JT direction (labeled O_{JT} hereafter) along the (101) plane (blue plane in Figure 2A).

Consistent with the above static band structure and band dynamics in reciprocal space, strong couplings of charge fluxes and lattice dynamics in real space are found in the δ^- state. When perturbing a pair of O_{JT} along the (101) plane or perturbing a $Mn^{3.5+}$ in a pair of $Mn^{3.5+}$ dimer ions along the *b* direction, which are the critical components of two important phonon modes to be discussed later, charge fluxes (f) are generated, as illustrated in Figure 2E, which can be analyzed from the charge density difference results (Figure S15). Because it will also be shown later that abnormal magnetic fluctuations are likely to be strongly correlated with such fluxes in the $Mn^{3.5+}O_6$ stripe region generated from these phonons, we now focus on analyzing the strength of fluxes inside (f_i) and outside (f_o) of the stripe region induced by different ion perturbations, as well as the flux confinement ratio $f_i/(f_i + f_o)$ of the stripe region (see Experimental procedures). We find that, under both perturbations in Figure 2E, strong fluxes are generated within the $Mn^{3.5+}$ stripe region (pink stripe in Figures 1B and 2E), whereas a small portion of charge flows to the neighboring $Mn^{3.5+}$ stripe or leaks to the $Mn^{3+/4+}$ stripe (stripe with mixed purple and grey hexagons).

We then extend the above flux analysis based on the perturbation of a single ion or a pair of ions to the perturbations from the entire phonon spectra for all of these structures in Figures 2F and 2G. Flux strength is thus analyzed within the entire $Mn^{3.5+}$ stripe region formed by all the parallel pink stripes in a supercell (Figure 2E), generated by each phonon mode, as shown by an individual grey dot in Figure 2F. The flux confinement ratio is also calculated in the same way based on fluxes within the entire $Mn^{3.5+}$ stripe region (i.e., f_i) or not (i.e., f_o), as shown in Figure 2G. We find that δ^- not only shows the strongest average fluxes (Figure 2F) but also a relatively high flux

Please cite this article in press as: Chen et al., Dynamically preferred state with strong electronic fluctuations from electrochemical synthesis of sodium manganate, Matter (2021), https://doi.org/10.1016/j.matt.2021.12.012

confinement ability of the stripe region (Figure 2G). This could be caused by the partially occupied non-narrow band near E_f that is also well separated from other bands, with the features also robust against ionic perturbation (Figures 2C and 2D). The partial occupancy and certain band width support a more collective and robust electron motion in response to phonons, whereas the separation from other bands prevents intermixing of electrons to other bands so that fluxes can be better confined in the top band that resides mainly in the $Mn^{3.5+}$ stripe region. This describes a unique picture of strong collective fluxes that are spatially confined in the $Mn^{3.5+}$ stripe region of the δ^- state at x = 1/2.

To further understand the influence of the unique band and flux dynamics of the δ^- state on the lattice dynamics and (dynamic) magnetic properties, we performed chemical desodiation from $NaMnO_2$ to create a clean and sufficient powder sample of $Na_{1/2}MnO_2$ for Raman and neutron measurements. The $NaMnO_2$ sample was synthesized and sintered in exactly the same way as the one used for electrochemical desodiation in the *in situ* SXRD measurement. The chemical desodiation of the powder sample was performed by soaking $NaMnO_2$ in a solution of iodine (see Experimental procedures), one of the gentlest oxidizers, for a much longer time than for electrochemical desodiation to reach $Na_{1/2}MnO_2$. These approaches are used to minimize any defects by chemical desodiation. SXRD measurement of the chemically desodiated $Na_{1/2}MnO_2$ powder shows a great match of structural details to the *in situ* SXRD pattern of Na_xMnO_2 at x = 1/2 (Figure S16).

Figure 3A shows the Raman spectra of electrochemically prepared $Na_{1/2}MnO_2$ cooling from room temperature to 10 K. Large frequency shifts with temperature are observed mainly for peaks at low and high frequencies, such as at 125 cm^{-1} and 400 cm^{-1} (Figure S17). The Raman peak shifts of the 16 clearly observable modes are shown in Figure 3B, with the effect of thermal expansion subtracted (see Experimental procedures). Many modes at less than 130 cm^{-1} and more than 300 cm^{-1} show strong peak shifts, suggesting a strong anomalous anharmonicity. Figure 3C presents the anharmonic phonon coupling strength G in DFT simulations between each pair of the 37 modes in the phonon spectrum of the δ^- state (see Experimental procedures). By comparing the experimental Raman spectra with the calculated phonon DOS (Figures S18 and S19), we find that strong couplings exist among a subset of modes in δ^-, including the four lowest-frequency modes 0–3 (<130 cm^{-1}) with the strongest Na movements and the higher frequency modes 13, 17, 22, 25, 28, 30, and 32 (>300 cm^{-1}) with majority Mn and O ion movements. Compared with all other structures (Figures 3D and S20), the δ^- state also shows the strongest coupling strength G that is outstanding among Na_xMnO_2, whereas the ground energy state v_0^- at x = 1/2 is actually one of the weakest. This also suggests that δ^--$Na_{1/2}MnO_2$ is preferred by anharmonic stabilization. Softening of the anharmonic phonon couplings here, on the other hand, is also likely to further decorate δ^- with subtle additional distortions in experiment.[14,25,26]

Temperature-dependent neutron diffraction of $Na_{1/2}MnO_2$ (Figures 4A, 4B, S21, and S22) shows a long-range magnetic ordering phase transition temperature T_N at 47 K. The magnetic peaks measured by neutron diffraction below T_N match the model shown in the inset of Figure 4A from neutron refinements. The refined magnetic structure is an antiferromagnet with the ordering wavevector $\mathbf{k}$ (*r.l.u.*) = (0, 0, $^1/_2$), where *r.l.u.* stands for reciprocal lattice unit. Hereafter, the magnetic peaks are referenced with respect to the magnetic unit cell, which is doubled along the c axis with respect to the nuclear unit cell. This magnetic ordering is also predicted by magnetic coupling constants J from DFT simulations as the ground-state magnetic structure of the δ^- state (Figure S23). The $J_{33}^{(1)}$ along the b stripe direction between two nearest $Mn^{3.5+}$ ions shows the strongest

Please cite this article in press as: Chen et al., Dynamically preferred state with strong electronic fluctuations from electrochemical synthesis of sodium manganate, Matter (2021), https://doi.org/10.1016/j.matt.2021.12.012

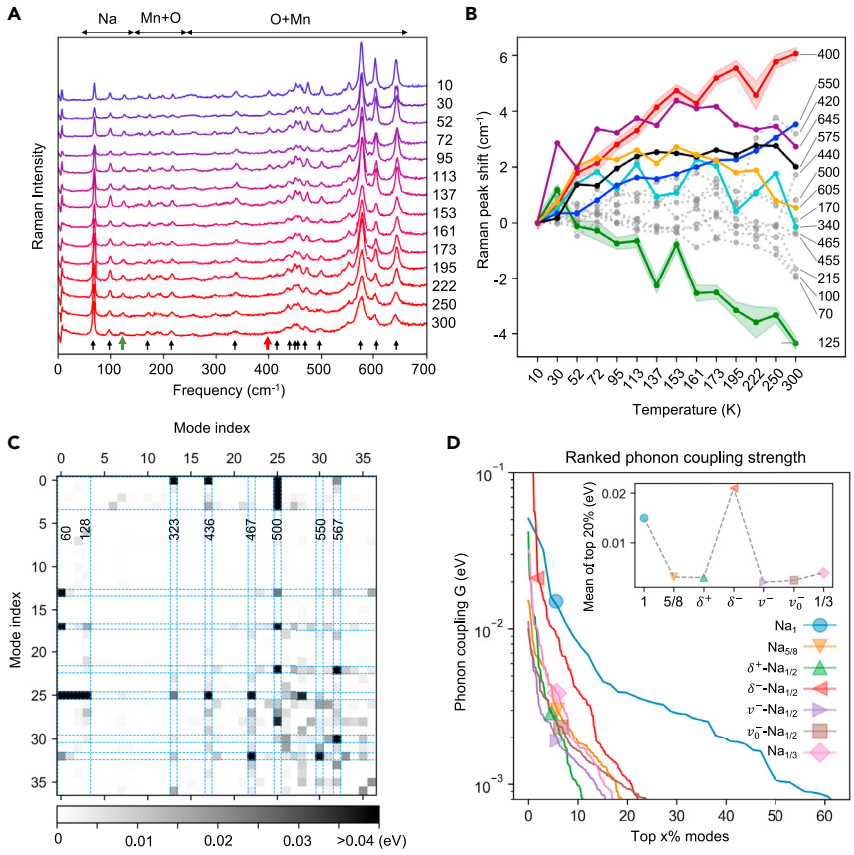

Figure 3. Strong anharmonic phonon coupling in $Na_{1/2}MnO_2$

(A) Raman measurements for $Na_{1/2}MnO_2$ cooling from 300 K to 10 K with the temperature in Kelvin of each spectrum labeled on the right. The 16 Raman peaks marked by black, green, and red arrows were selected for further analysis. Green and red arrows indicate two Raman peaks with significant shifts in frequency with decreasing temperature (Figure S17). Three typical frequency ranges dominated by different phonon modes were determined by comparing with DFT simulations and are labeled at the top, with Na modes at low frequencies, Mn-dominant modes mixed with minor oxygen modes at intermediate frequencies (Mn + O), and O-dominant modes mixed with minor Mn modes (O + Mn) at high frequencies.

(B) Raman peak frequency shift with temperature, relative to the value at 10 K, for peaks marked in (A). The frequency in cm^{-1} of each peak at 10 K is labeled on the right. The volume expansion effect has been subtracted. The shaded regions represent the standard deviation from measurements and peak position calculations. Many modes with frequencies of more than 300 cm^{-1} involve a positive peak shift in certain temperature ranges.

(C) Nonlinear phonon coupling between 37 modes of the δ^- state. A darker grey scale indicates stronger phonon coupling. The blue dashed stripes mark the modes with strongest anharmonic phonon couplings to other modes, with their frequencies (in cm^{-1}) labeled. The phonon coupling maps for all seven Na_xMnO_2 states are shown in Figure S20.

(D) Comparison of the phonon coupling spectra of all seven Na_xMnO_2. The mode pairs are ranked from highest to lowest phonon coupling strength G for each state. The markers indicate the average phonon coupling strength of the top 20% mode pairs for each state, which are summarized in the inset.

ferromagnetic (FM) coupling that dominates the FM *b* stripe ordering, where the superscript (1) represents the nearest-neighbor Mn-Mn interaction, and the subscript 3 represents the valence of Mn (which is just a notion and should not be taken as exact here because the valence suggested by DFT is around 3.5+). The abnormal JT distortions of weakly compressed $Mn^{3.5+}O_6$ in the δ^- state (Figures 1C and S11) may cause the FM coupling of $J_{33}^{(1)}$, whereas $Na_{5/8}MnO_2$[7] and the δ^+ state at x = 1/2 with strongly

Please cite this article in press as: Chen et al., Dynamically preferred state with strong electronic fluctuations from electrochemical synthesis of sodium manganate, Matter (2021), https://doi.org/10.1016/j.matt.2021.12.012

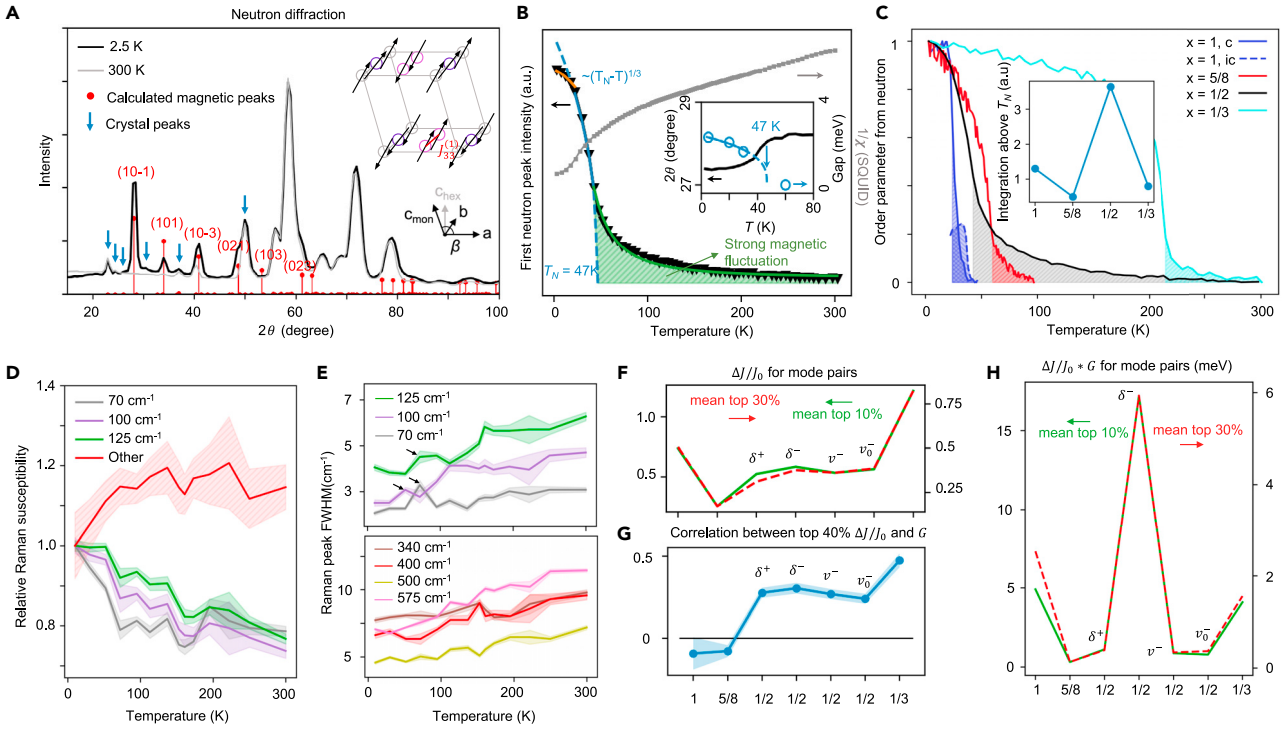

Figure 4. Strong magnetic fluctuations synchronized with anharmonic phonon couplings in $Na_{1/2}MnO_2$

(A) Neutron diffraction patterns at 2.5 K (black) and 300 K (grey). Calculated magnetic peaks are labeled by red lines. The inset illustrates the magnetic moments obtained from neutron diffraction refinement. Major crystal peaks are labeled by blue arrows. The magnetic unit cell consists of two layers of Mn spins with AFM interlayer stacking.

(B) Energy integrated intensity (black triangle), including magnetic fluctuations (green area), of the (10-1) strongest magnetic peak (left scale) and the inverse magnetic susceptibility (grey line, right scale) versus temperature. The order parameter of the region right below T_N is fitted with the $(T_N-T)^{1/3}$ power law (blue dashed line). See also Figure S22 for the order parameter fit. The inset shows the weighted average (10-1) peak position (black line) and the magnon gap (blue circle) measured by inelastic neutron scattering (Figure S25), both versus temperature.

(C) Order parameters from neutron diffraction versus temperature compared among Na_xMnO_2 for x = 1, 5/8, 1/2, and 1/3. The inset shows a comparison of the integrated shade area above T_N. The x = 1, 5/8, and 1/3 data are reproduced from Li et al.,[7] Dally et al.,[10] and Chen et al.,[7,10,20] respectively. Both commensurate (c) and incommensurate (ic) residue intensities are integrated for the inset point at x = 1.

(D) Raman susceptibility versus temperature. The shaded regions for the bottom three modes represent the error bar. The shaded region with red lines marks the range of all other high-frequency modes.

(E) Full-width half-maximum (FWHM) of two groups of Raman peaks around low (top plot) and high (bottom plot) frequencies, respectively, versus temperature. The shaded region corresponds to the error.

(F) The strongest relative J change, $\Delta J/J_0$, induced by any pairs of phonon modes at zero point amplitude.

(G) Correlation between mode pairs with the top 40% $\Delta J/J_0$ and G for each structure. The shaded area shows the error bar of the correlation.

(H) The product of $\Delta J/J_0$ and corresponding phonon coupling strength G.

(F) and (H) compare the δ^- state with all other Na_xMnO_2 for the mean top 10% (green) and 30% (red) mode pairs.

elongated JT distortions instead prefer antiferromagnetic (AFM) $J_{33}^{(1)}$ couplings along similar stripe patterns in our DFT simulations. The δ^+ state thus gives a very different magnetic structure from DFT prediction that cannot be refined by the neutron diffraction data. Therefore, the magnetic structure from neutron diffraction measurement of $Na_{1/2}MnO_2$ at low temperature below T_N provides strong evidence to include the δ^- state while simultaneously helping exclude the δ^+ state. In addition, the neutron diffraction and neutron PDF measurements at room temperature also show obviously better refinement goodness of fit for δ^- , with R_{wp} = 11.1% (diffraction) and 15.9% (PDF) compared with the 14.0% and 17.9%, respectively, of δ^+ (Figure S24).

The transition temperature T_N obtained from fitting the intensity of the (10-1) magnetic peak versus temperature matches well with the inflection point in the inverse

Please cite this article in press as: Chen et al., Dynamically preferred state with strong electronic fluctuations from electrochemical synthesis of sodium manganate, Matter (2021), https://doi.org/10.1016/j.matt.2021.12.012

magnetic susceptibility from Superconducting Quantum Interference Device (SQUID) measurement (Figure 4B). The inset shows that, near T_N, the weighted average peak position has a sudden shift toward a higher angle, and the magnon gap measured by inelastic neutron scattering disappears (Figure S25). Above T_N, however, significant neutron intensity remains and decreases slowly with temperature, indicating strong magnetic fluctuations above the magnetic long-range-ordered state, in a very wide temperature range. In comparison, such remaining neutron intensity of Na_xMnO_2 at other Na compositions decays quickly above T_N (Figure 4C).[7,10,11,20] The integrated residue intensities from T_N to high temperatures highlight the anomaly of $Na_{1/2}MnO_2$ (Figure 4C inset), which is about 3 times larger than that of $NaMnO_2$ with well known spin fluctuations because of low dimensionality or geometric frustration[9–12] and more than 7 times larger than that of $Na_{5/8}MnO_2$ with a similar 1D stripe pattern (Figure 1B). Note that, especially for x = 1/3[20] and x = 5/8,[7] the Na_xMnO_2 powder was synthesized and chemically desodiated in exactly the same way by us as x = 1/2, and the neutron diffraction was performed on the same instrument and using the same measurement configuration. Therefore, we believe that the unique strong magnetic fluctuation observed in $Na_{1/2}MnO_2$ reflects certain intrinsic changes from other Na compositions rather than being caused by trivial factors, such as defects generated in synthesis.

Raman measurements of $Na_{1/2}MnO_2$ further reveal anomalies around T_N, suggesting strong magnon-phonon coupling. For some Na modes at low frequencies, the Raman susceptibility quickly increases with decreasing temperature below T_N, whereas the change is noticeably slower above T_N (Figure 4D). For other high-frequency modes, an opposite trend is observed. For the Raman peak full-width half-maximum (FWHM) versus temperature, the Na modes all have a bump around 50–70 K, whereas such an anomaly cannot be found in other modes (Figure 4E). DFT simulations further show that, dynamically, the value of $J_{33}^{(1)}$ is very susceptible to and also strongly coupled to phonon oscillations in the δ^- state. We first use two strongly coupled modes as an example to illustrate this effect before the demonstration using the entire phonon spectrum. With increasing phonon amplitude of the dimer mode (22) or O_{JT} mode (25), as illustrated in Figure S26A, the $J_{33}^{(1)}$ changes from FM toward AFM couplings, with the general trend proportional to the phonon induced difference in magnetic moments between the two neighboring $Mn^{3.5+}$ ions in the stripe region. The strong anharmonic phonon coupling between the two modes further leads to faster change of $J_{33}^{(1)}$ to become AFM (black dots in Figure S26B), just above the zero-point amplitude. Note that our phonon simulations show that, at around T_N (47 K), the average ion oscillation amplitude already reaches 1.5 times that at 0 K (Figure S27). Thus, strongly coupled phonons in the δ^- state exhibit the ability to fluctuate the dominant magnetic exchanges between FM and AFM couplings above T_N.

Such DFT simulations are then extended to all possible phonon pairs. We rank the relative change of magnetic coupling constants, $\Delta J/J_0$, caused by all phonon mode pairs of each Na_xMnO_2 structure and present their converged mean top values in Figure 4F. We then calculate the correlation of this $\Delta J/J_0$ rank with the previous G rank (Figure 3D and inset) for each structure, which is an indicator of how likely it is that a strongly coupled phonon pair will also generate a strong change of magnetic coupling in any Na_xMnO_2 structure (Figure 4G), where an extra 10% in both ranks is included for the accuracy of the correlation calculation. Finally, the metric of $\Delta J/J_0 \cdot G$ most relevant to the electronic dynamics in Na_xMnO_2 is presented in Figure 4H, which shows that the effect of coupled lattice and magnetic dynamics is indeed the most magnificent in the δ^- state compared with other Na_xMnO_2 states, matching well with the trend of magnetic fluctuation strength along x = 1, 5/8, 1/2,

Please cite this article in press as: Chen et al., Dynamically preferred state with strong electronic fluctuations from electrochemical synthesis of sodium manganate, Matter (2021), https://doi.org/10.1016/j.matt.2021.12.012

1/3 in the neutron analysis in Figure 4C, inset. Although $NaMnO_2$ shows a relatively strong G (Figure 3D, inset), it lacks the correlation with $\Delta J/J_0$ (Figure 4G). Although $Na_{1/3}MnO_2$ does show a large $\Delta J/J_0$ and a high correlation to G, its phonon coupling strength G, however, is too low (Figure 3D, inset). Therefore, the metric that calculates $\sum_i \Delta J_i/J_0 \Delta G_i$ here actually requires both to be strong and to happen simultaneously, which is only found in the thermodynamically unstable δ^--$Na_{1/2}MnO_2$ state, which, however, is preferred by anharmonic stabilization in experiment.

The above analysis also emphasizes the importance of the δ^- state compared with the other states of v_0^-, v^-, and δ^+ at x = 1/2 in contributing to the strong magnetic fluctuation observed in neutron order parameter analysis of $Na_{1/2}MnO_2$. Compared with δ^-, the v_0^-, v^-, and δ^+ states can also be considered silent states in terms of magnetic fluctuations (Figure 4H). However, it is worth noting that, although the δ^+ state has been largely excluded by the magnetic long-range ordering structure analysis, together with the worse neutron diffraction and neutron PDF refinement compared with the δ^- state, the remaining two states of v_0^- and v^- at x = 1/2 cannot be fully excluded. They show SXRD (Figure S11) and neutron diffraction (Figure S28) refinement results similar to the δ^-state. Also, their magnetic couplings along the b direction are FM as well, which is the same as δ^-, so the magnetic ordering structure suggested by neutron magnetic diffraction refinement cannot exclude v_0^- or v^- either. Considering that they are silent in magnetic fluctuation and that v_0^- is actually the DFT ground energy state, including them together with the δ^- state in $Na_{1/2}MnO_2$ will not violate known experimental facts here. That said, the opposite is not true; that is, excluding the δ^- state will lose the flux, magnetic, and lattice dynamics that are unique to δ^- and required by the synergy between our experimental and computational data. We thus also performed two-phase refinements of $Na_{1/2}MnO_2$ neutron diffraction data for $\delta^- + v_0^-$ and $\delta^- + v^-$, which shows an improved goodness of fit for R_{wp} from around 11% for the δ^-, v_0^-, or v^- individual phase to around 7.5% for the two phases (Figure S28). This suggests that the possibility of two-phase coexistence, or an even larger supercell that orders alternating regions representing the two phases, should not be excluded.

Specifically, if we go beyond the primitive cell size defined by the four DFT low-energy states, then a larger supercell with alternating δ^- and v_0^- or v^- regions can be constructed. This approach is actually important for enabling the superstructure XRD to match the small XRD peak at 4.7° (Figure S16), which does not correspond to any set of (hkl) planes in the primitive cell of the four low-energy states of v_0^-, v^-, δ^-, and δ^+. Our crystallographic analysis shows that it requires a supercell with at least doubled primitive cell size in the b direction. For example, in a supercell with four times in the a direction and two times in the b direction (Figure S29), our DFT simulation shows that the δ^- type and the mixed ν^-/ v_0^- (or simply mixed ν) type block regions alternating along the a direction can coexist, where the dynamically important $Mn^{3.5+}$ stripe in the δ^- state can be maintained in periodic block regions, while the mixed νrelated regions are still dynamically silent. Note that such an unusually large supercell is not uncommon in the Na_xMnO_2 system and has been found before in $Na_{5/8}MnO_2$.[7] This $Na_{1/2}MnO_2$ structure, illustrated in Figure S29, together with many other structures with such combinations along either a or b direction of δ^-, ν^-, and v_0^- block regions we checked, all can fit this 4.7° peak, with one example shown in Figure S30 for comparison between XRD simulations, refinements, and experiments. Although further resolving the exact large supercell structure that combines the several DFT low-energy states for $Na_{1/2}MnO_2$ could be complicated and requires more advanced characterizations and computations, the

Please cite this article in press as: Chen et al., Dynamically preferred state with strong electronic fluctuations from electrochemical synthesis of sodium manganate, Matter (2021), https://doi.org/10.1016/j.matt.2021.12.012

analysis here, nevertheless, emphasized the inclusion of the dynamically preferred δ^- state region as the main focus of this work.

Conclusion

The strong collective flux confined in the $Mn^{3.5+}O_6$ stripe region unique to δ^--$Na_{1/2}MnO_2$ is likely to play a critical role here. Such directional fluxes originated from the collective dynamics of electrons and lattices (i.e., f^d), may effectively transfer the energy of anharmonic phonon coupling G to transiently modulate the magnitude or even flip the sign of dominant magnetic coupling constants J, causing a big ΔJ in a wide temperature range above T_N, with G and ΔJ controlled simultaneously by f^d. This results in certain nontrivial functional relationships of $\Delta J(f^d)$ and $G(f^d)$, interacting mainly through the entire transient distribution of the f^d function in the crystal. This emphasizes the physical significance of the dynamic charge flux functionals over the static charge density functionals to such a dynamically preferred state created by electrochemical processes. Our work will provide a new perspective to understand the relationship between strong electronic fluctuations, functionalities, and structure instabilities, making it potentially relevant to other novel quantum states, where high conversion efficiency can be found in perovskite solar cell materials at metastable and unstable states,[14] and novel superconducting related properties can emerge from nickelates near such structure instability from electrochemical synthesis.[15]

EXPERIMENTAL PROCEDURES

Resource availability

Lead contact

The lead contact is Xin Li (lixin@seas.harvard.edu).

Materials availability

This study did not generate new unique materials. For synthesis of Na_xMnO_2, please refer to the Synthesis section.

Data and code availability

The datasets generated during the current study are available from the corresponding author upon reasonable request. Relevant crystal structure files are available on The Cambridge Crystallographic Data Centre (CCDC) associated with the DOI of this paper (https://doi.org/10.1016/j.matt.2021.12.012).

The code to analyze the data is available from the corresponding author upon reasonable request.

Synthesis

Pristine $NaMnO_2$, $NaNiO_2$, and $NaCoO_2$ powder was synthesized by solid-state reactions following previous publications.[19,27,28] The $Na_{1/2}MnO_2$ powder for the neutron diffraction and PDF measurement was obtained by chemical deintercalation of pristine $NaMnO_2$ powder in an iodine acetonitrile solution with a 3:1 molar ratio of iodine over Na, reacted for 24 h at room temperature in a glovebox. The chemically desodiated $Na_{1/2}MnO_2$ was confirmed to be free from impurity phase or structure disorder by matching its SXRD profile with the profile of $Na_{1/2}MnO_2$ from *in situ* SXRD (Figure S16). The cathode film of $Na_{1/2}MnO_2$ for Raman measurements was obtained by an electrochemical method[27] with a C/50 charging rate until reaching the ~3.0 V plateau, which corresponds to the strongest $Na_{1/2}MnO_2$ ordering recorded in *in situ* XRD.

Please cite this article in press as: Chen et al., Dynamically preferred state with strong electronic fluctuations from electrochemical synthesis of sodium manganate, Matter (2021), https://doi.org/10.1016/j.matt.2021.12.012

(*In-situ*) SXRD

In situ SXRD experiments were performed at the powder diffraction beamline, 11-BM, at the Advanced Photon Source at Argonne National Laboratory. High-angular-resolution XRD data were collected using a 12-channel analyzer detector array (λ = 0.413609 Å; beam size, 1.5 × 0.5 mm). Data spanning a 0°–26° 2θ range were collected using a step size of 0.002°. Measurements were taken at C/50 rate[20] at every 2-h interval with a 30-min scan time for each pattern, corresponding to a 4% Na composition interval between patterns and 1% Na composition resolution per pattern. *Ex situ* SXRD measurements on chemically desodiated $Na_{1/2}MnO_2$ were performed in a sealed capillary and collected at beamline 28-ID-2 of the National Synchrotron Light Source II at Brookhaven National Laboratory, using a photon wavelength of 0.1844 Å. An amorphous silicon flat-panel two-dimensional detector (PerkinElmer) was used, and the raw image data were radially integrated using Fit2D software. The beam size used in this work was 1 × 1 mm. Rietveld refinements were performed within the Topas software. The backgrounds of XRD patterns are approximated by Chebyshev polynomials of order 30.

Neutron diffraction, neutron PDF, and magnetic susceptibility

Neutron diffraction measurements were performed on 5 g of chemically deintercalated $Na_{1/2}MnO_2$ powder using the triple-axis spectrometer BT-7[29] at the National Institute of Standards and Technology (NIST) Center for Neutron Research. A closed cycle He refrigerator with a base temperature of 2.5 K was employed, using a wavelength of 2.359 Å and a position-sensitive detector. Inelastic measurements to determine the spin gap were taken on the SPINS cold neutron spectrometer with a fixed final energy of 5 meV. Heatmap neutron measurements were swept at 10 K/min within each 5 K temperature step with each measurement of 5 min at a given temperature, giving around 6 h of total measurement time from 300 K to 2.5 K. The calculation of the intensity of the neutron scattering uses the formula $|F(hkl)|^2/(sin\theta sin2\theta)$, where F is the structure factor of the product of collinear spin and a phase factor $\exp(-2\pi i(hx + ky + lz))$, and (x,y,z) is the coordinate of each Mn ion. 2θ is the scattering angle. The magnetic susceptibility measurements were obtained using a Quantum Design MPMS-3 SQUID at 20 Oe in DC mode (1 Oe = 1,000/4π A/m), with a sweep rate of 4 K/min within each 2 K temperature step, giving around 5 h of total measurement time for a Zero Field Cooling (ZFC) or Field Cooling (FC) mode between 300 K and 1.8 K.

The chemically deintercalated $Na_{1/2}MnO_2$ powder was also sealed in capillaries for neutron diffraction and nPDF measurements at room temperature at the Nanoscale-Ordered Materials Diffractometer (NOMAD) beamline at the Spallation Neutron Source, Oak Ridge National Laboratory, one of the fastest neutron diffractometers in the world.[30,31] The high neutron flux and large detector enable the use of only a 0.3-g powder sample, which was loaded into thin-walled quartz capillary (diameter of 3 mm). Four 24-min scans were collected and summed to improve the statistics. Signal from empty quartz capillary was subtracted, with the obtained intensity normalized to correct for detector efficiency, and the absorption and multiple scattering were corrected. For the reduction of nPDF data, inelasticity polynomial correction of the self-scattering was performed. The normalized distinct scattering function (SQ-1) was Fourier transformed to obtain the reduced PDF G(r) with a Q_{max} cutoff of 35 $Å^{-1}$. The neutron diffraction structure refinements were carried out using Topas v.6 software. Time of flight (TOF) was converted to d-spacing using a conventional second-order polynomial. For the low-resolution frames (banks 2 and 3), a back-to-back exponential function convoluted with a symmetrical Gaussian function was used to describe the peak profile. For the high-resolution frames (banks 4 and 5), the moderator-induced line profile was modeled using a modified Ikeda-Carpenter-David function.[32–34] Lorentz

Please cite this article in press as: Chen et al., Dynamically preferred state with strong electronic fluctuations from electrochemical synthesis of sodium manganate, Matter (2021), https://doi.org/10.1016/j.matt.2021.12.012

polarization is corrected by multiplying d.[4] For nPDF analysis, the instrument constants Q_{broad} and Q_{damp} were determined from refinement of a Si standard to be 0.19 $Å^{-1}$ and 0.21 $Å^{-1}$, respectively.

Raman measurements

The Raman measurements were performed using an airtight sample holder with an electrochemically prepared $Na_{1/2}MnO_2$ cathode film loaded in an Ar-filled glovebox before transferring it to the Raman spectrometer.[35] To avoid damaging and overheating the artifact, the presented data, using a laser power of 15 μW, were double checked with the data at 5 μW. A 5 K/min temperature sweep rate was used to reach a neighboring temperature, and ~1.5 K/min was used to reach the actual temperature. It takes less than an extra 5 min to reach near equilibrium before the first measurement at each temperature. Three Raman scans at each temperature were measured to make sure there was no drifting of laser spot in the last two scans to guarantee the temperature stability in the third scans reported in Figure 3A. Each Raman spectrum measurement takes 20 min. The entire cooling measurement from 300 K to 10 K took around 25.5 h. In Figure 3B, an estimated volume thermal expansion coefficient of 10^{-5} K^{-1}[36] was used. The Grüneisen parameter is 1.0 according to our DFT calculation. Raman susceptibility[37] is calculated from $\chi_R(T)/\chi_R(10\ K)$, where $\chi_R(T) = I/(n_B+1)$, with $n_B = exp(-\hbar\omega/k_BT)$ as the Bose factor and I as the intensity of the Raman peak.

DFT

All DFT calculations in this work were performed using the Vienna *ab initio* Simulation Package (VASP) within the projector augmented wave (PAW) approach using the Perdew-Burke-Ernzerhof generalized gradient approximation (GGA) functional and the GGA + U extension to it. The U value for Mn is 3.9 eV, in line with previous studies.[20] A 520-eV plane-wave energy cutoff was used for all calculations. The Brillouin zone was sampled using centered Monkhorst-Pack meshes with a density of at least 28 Å along each reciprocal lattice vector. Forces were converged within to 0.01 eV/Å. The ground-state structure and energy of each stacking phase at each Na composition in the $NaNiO_2$ phase diagram (Figure S10) was obtained by DFT relaxation of the 30 Na orderings with the lowest Ewald energies. The lattice parameters were fully relaxed, and the DFT-D3BJ van der Waals correction is employed. The number of oxygen ions in $Mn^{3+}O_6$ is proportional for x = 1/2 and x = 5/8 but not for x = 1/3 because in x = 1/3 there is no edge sharing between $Mn^{3+}O_6$. To normalize, the flux contribution from oxygen in x = 1/3 is scaled by a factor of 2/3 to make it proportional to the other cases. In the charge flux calculation, the direction of the flux is determined using the information of the total charge difference and charge distribution change of each ion as well as local symmetry constraints. The $Mn^{3+}O_6$ octahedra are defined as in stripe, and other ions are defined as out of stripe. The charge confinement ratio was thus calculated based on the charge of ions obtained by integrating the site-decomposed DOS over the group of bands below the Fermi level, as described in Figure S13. The calculation of magnetic coupling and ground state was based on an Ising-like model, where the total energy is $E = -\sum_{<i,j>} J_{ij}\sigma_i\sigma_j$ with all possible J_{ij} up to the third nearest neighbor. σ_i takes a value of ± 1, corresponding to the "spin-up" and "spin-down" states. Phonon calculations were performed with enlarged supercells containing at least 32 formula units of Na_xMnO_2 with at least 10 Å in each lattice dimension. For example, the calculation for $Na_{1/2}MnO_2$ uses a supercell of 2*2*2 = 8 copies of the monoclinic unit cell of the $Na_{1/2}MnO_2$, which has 4 formula units of $Na_{1/2}MnO_2$ (Figure 2A). The anharmonic phonon coupling calculation follows the previous method.[13,38] The phonon calculations were performed in the framework of the Phonopy software.[39]

SUPPLEMENTAL INFORMATION

Supplemental information can be found online at https://doi.org/10.1016/j.matt.2021.12.012.

ACKNOWLEDGMENTS

This work was supported by the Dean's competitive fund of promising scholarship at FAS at Harvard University and a Harvard Data Science Initiative Competitive Research Award. Y.W. and K.B. acknowledge primary support from the US Department of Energy (DOE), Office of Science, Office of Basic Energy Sciences under award DE-SC0018675. Computations were supported by computational resources from the Texas Advanced Computing Center (TACC) and the Odyssey cluster supported by the FAS Division of Science, Research Computing Group at Harvard University. This work also made use of the Shared Experimental Facilities supported in part by the Materials Research Science and Engineering Centers (MRSEC) Program of the National Science Foundation under award DMR-1419807. Use of the Advanced Photon Source at Argonne National Laboratory was supported by the DOE, Office of Science, Office of Basic Energy Sciences, under contract DE-AC02-06CH11357. The identification of any commercial product or trade name does not imply endorsement or recommendation by the National Institute of Standards and Technology. The work done at BNL is supported by the Assistant Secretary for Energy Efficiency and Renewable Energy, Vehicle Technology Office of the DOE through the Advanced Battery Materials Research (BMR) Program under contract DE-SC0012704. This research used beamline 28-ID-2 of the NSLS II, a DOE Office of Science user facility operated for the DOE Office of Science by BNL under contract DE-SC0012704. The neutron diffraction studies at NOMAD used resources at the Spallation Neutron Source, a DOE Office of Science User Facility operated by ORNL.

AUTHOR CONTRIBUTIONS

X.L. conceived the project and planned the research. X.C. performed the DFT calculations. Yichao Wang synthesized $NaMnO_2$, $NaCoO_2$, and $NaNiO_2$ powder samples for *in situ* SXRD and prepared the chemically desodiated $Na_{1/2}MnO_2$ for neutron and Raman measurements. Yiping Wang and K.B performed Raman setup and measurements, and Yichao Wang and X.C. assisted with remote monitoring during the measurements. R.L.D. and J.W.L. performed the temperature-dependent neutron diffraction and inelastic neutron scattering measurements, analyzed inelastic neutron scattering data, and performed the magnetic structure refinement. X.L. and K.W performed the *in situ* synchrotron XRD measurements. T.Q. obtained the phonon modes, DOS, and temperature-dependent oscillation amplitudes from DFT calculations. J.L. performed the neutron diffraction and neutron PDF measurements at room temperature and the structural refinements. E.H. performed the *ex situ* synchrotron XRD measurements. X.C. and X.L. analyzed the experimental data with the help of discussions with all authors. X.C. and X.L. analyzed the computational and experimental results and wrote the manuscript. X.L. conceived the physical picture of entangled magnetic and lattice dynamics through charge flux functionals.

DECLARATION OF INTERESTS

The authors declare no competing interests.

Received: September 19, 2021
Revised: November 18, 2021
Accepted: December 13, 2021
Published: January 5, 2022

REFERENCES

1. Yabuuchi, N., Kubota, K., Dahbi, M., and Komaba, S. (2014). Research development on sodium-ion batteries. Chem. Rev. *114*, 11636–11682.
2. Ortiz-Vitoriano, N., Drewett, N.E., Gonzalo, E., and Rojo, T. (2017). High performance manganese-based layered oxide cathodes: overcoming the challenges of sodium ion batteries. Energy Environ. Sci. *10*, 1051–1074.
3. Delmas, C., Carlier, D., and Guignard, M. (2021). The Layered oxides in lithium and sodium-ion batteries: a solid-state chemistry approach. Adv. Energy Mater. *11*, 2001201.
4. Guignard, M., Didier, C., Darriet, J., Bordet, P., Elkaïm, E., and Delmas, C. (2013). P2-Na_xVO_2 system as electrodes for batteries and electron-correlated materials. Nat. Mater. *12*, 74–80.
5. Roger, M., Morris, D.J.P., Tennant, D.A., Gutmann, M.J., Goff, J.P., Hoffmann, J.U., Feyerherm, R., Dudzik, E., Prabhakaran, D., Boothroyd, A.T., et al. (2007). Patterning of sodium ions and the control of electrons in sodium cobaltate. Nature *445*, 631–634.
6. Takada, K., Sakurai, H., Takayama-Muromachi, E., Izumi, F., Dilanian, R.A., and Sasaki, T. (2003). Superconductivity in two-dimensional CoO_2 layers. Nature *422*, 53–55.
7. Li, X., Ma, X., Su, D., Liu, L., Chisnell, R., Ong, S.P., Chen, H., Toumar, A., Idrobo, J.C., Lei, Y., et al. (2014). Direct visualization of the Jahn-Teller effect coupled to Na ordering in $Na_{5/8}MnO_2$. Nat. Mater. *13*, 586–592.
8. Chen, X., Tang, H., Wang, Y., and Li, X. (2021). Balancing orbital effects and on-site Coulomb repulsion through Na modulations in Na_xVO_2. Phys. Rev. Mater. *5*, 084402.
9. Stock, C., Chapon, L.C., Adamopoulos, O., Lappas, A., Giot, M., Taylor, J.W., Green, M.A., Brown, C.M., and Radaelli, P.G. (2009). One-dimensional magnetic fluctuations in the spin-2 triangular lattice α−$NaMnO_2$. Phys. Rev. Lett. *103*, 077202.
10. Dally, R.L., Chisnell, R., Harriger, L., Liu, Y., Lynn, J.W., and Wilson, S.D. (2018). Thermal evolution of quasi-one-dimensional spin correlations within the anisotropic triangular lattice of α-$NaMnO_2$. Phys. Rev. B *98*, 144444.
11. Giot, M., Chapon, L.C., Androulakis, J., Green, M.A., Radaelli, P.G., and Lappas, A. (2007). Magnetoelastic coupling and symmetry breaking in the frustrated antiferromagnet α−$NaMnO_2$. Phys. Rev. Lett. *99*, 247211.
12. Zorko, A., El Shawish, S., Arčon, D., Jagličić, Z., Lappas, A., Van Tol, H., and Brunel, L.C. (2008). Magnetic interactions in α−$NaMnO_2$: quantum spin-2 system on a spatially anisotropic two-dimensional triangular lattice. Phys. Rev. B *77*, 024412.
13. Chen, X., Dong, J., and Li, X. (2020). A picture of pseudogap phase related to charge fluxes. Npj Comput. Mater. *6*, 1–12.
14. Bechtel, J.S., and Van Der Ven, A. (2018). Octahedral tilting instabilities in inorganic halide perovskites. Phys. Rev. Mater. *2*, 025401.
15. Li, D., Lee, K., Wang, B.Y., Osada, M., Crossley, S., Lee, H.R., Cui, Y., Hikita, Y., and Hwang, H.Y. (2019). Superconductivity in an infinite-layer nickelate. Nature *572*, 624–627.
16. Bussmann-Holder, A., Bishop, A.R., Migliori, A., and Fisk, Z. (1992). Role of structural instability in high-temperature superconductivity and its effect on isotope effect. Ferroelectrics *128*, 105–110.
17. Bersuker, B.I. (2006). The Jahn–Teller Effect (Cambridge Univ. Press).
18. Goodenough, J.B. (1998). Jahn-Teller phenomena in solids. Annu. Rev. Mater. Sci. *28*, 1–27.
19. Delmas, C., Braconnier, J.-J., Fouassier, C., and Hagenmuller, P. (1981). Electrochemical intercalation of sodium in Na_xCoO_2 bronzes. Solid State Ionics *34*, 165–169.
20. Chen, X., Wang, Y., Wiaderek, K., Sang, X., Borkiewicz, O., Chapman, K., LeBeau, J., Lynn, J., and Li, X. (2018). Super charge separation and high voltage phase in Na_xMnO_2. Adv. Funct. Mater. *28*, 1805105.
21. Kaufman, J.L., and Van Der Ven, A. (2019). Na_xCoO_2 phase stability and hierarchical orderings in the O3/P3 structure family. Phys. Rev. Mater. *3*, 015402.
22. Toumar, A.J., Ong, S.P., Richards, W.D., Dacek, S., and Ceder, G. (2015). Vacancy ordering in O3-type layered metal oxide sodium-ion battery cathodes. Phys. Rev. Appl. *4*, 064002.
23. de Boisse, B.M. (2014). Structural and Electrochemical Studies of $Na_xMn_{1-y}Fe_yO_2$ and $NaNiO_2$ Materials as Positive Electrode for Na-Ion Batteries (Université de Bordeaux)).
24. Braconnier, J.J., Delmas, C., and Hagenmuller, P. (1982). Etude par desintercalation electrochimique des systemes Na_xCrO_2 et Na_xNiO_2. Mater. Res. Bull. *17*, 993–1000.
25. Zhong, W., Vanderbilt, D., and Rabe, K.M. (1994). Phase transitions in $BaTiO_3$ from first principles. Phys. Rev. Lett. *73*, 1861–1864.
26. Cohen, R.E. (1992). Origin of ferroelectricity in perovskite oxides. Nature *358*, 136–138.
27. Ma, X., Chen, H., and Ceder, G. (2011). Electrochemical properties of monoclinic $NaMnO_2$. J. Electrochem. Soc. *158*, 1307–1312.
28. Vassilaras, P., Ma, X., Li, X., and Ceder, G. (2013). Electrochemical properties of monoclinic $NaNiO_2$. J. Electrochem. Soc. *160160*, 207–211.
29. Lynn, J.W., Chen, Y., Chang, S., Zhao, Y., Chi, S., Ratcliff, W., Ueland, B.G., and Erwin, R.W. (2012). Double-focusing thermal triple-axis spectrometer at the NCNR. J. Res. Natl. Inst. Stand. Technol. *117*, 61–79.
30. Neuefeind, J., Feygenson, M., Carruth, J., Hoffmann, R., and Chipley, K.K. (2012). The nanoscale ordered materials diffractometer NOMAD at the spallation neutron source SNS. Nucl. Instr. Methods Phys. Res. Sect. B Beam Interact. Mater. Atoms *287*, 68–75.
31. Calder, S., An, K., Boehler, R., Dela Cruz, C.R., Frontzek, M.D., Guthrie, M., Haberl, B., Huq, A., Kimber, S.A., Liu, J., et al. (2018). A suite-level review of the neutron powder diffraction instruments at Oak Ridge National Laboratory. Rev. Sci. Instrum. *89*, 092701.
32. Ikeda, S., and Carpenter, J.M. (1985). Wide-energy-range, high-resolution measurements of neutron pulse shapes of polyethylene moderators. Nucl. Instr. Methods Phys. Res. Sect. A Accel. Spectrometers, Detect. Assoc. Equip. *239*, 536–544.
33. Larson, A.C., and Von Dreele, R.B. (1994). Report LAUR, 86-748 (Los Alamos National Laboratory).
34. Young, R.A. (1993). The Rietveld Method (Oxford university press).
35. Wang, Y., Osterhoudt, G.B., Tian, Y., Lampen-Kelley, P., Banerjee, A., Goldstein, T., Yan, J., Knolle, J., Ji, H., Cava, R.J., et al. (2020). The range of non-Kitaev terms and fractional particles in α-$RuCl_3$. NPJ Quan. Mater *5*, 1–8.
36. Kobayashi, W., Yanagita, A., Akaba, T., Shimono, T., Tanabe, D., and Moritomo, Y. (2018). Thermal expansion in layered Na_xMO_2. Sci. Rep. *8*, 3988.
37. Tian, Y., Jia, S., Cava, R.J., Zhong, R., Schneeloch, J., Gu, G., and Burch, K.S. (2017). Understanding the evolution of anomalous anharmonicity in $Bi_2Te_{3-x}Se_x$. Phys. Rev. B *95*, 094104.
38. Kim, S., Chen, X., Fitzhugh, W., and Li, X. (2018). Apical charge flux-modulated in-plane transport properties of cuprate superconductors. Phys. Rev. Lett. *121*, 157001.
39. Togo, A., and Tanaka, I. (2015). First principles phonon calculations in materials science. Scr. Mater. *108*, 1–5.